Mechanics Research Communications 129 (2023) 104089

Contents lists available at ScienceDirect

Mechanics Research Communications

journal homepage: www.elsevier.com/locate/mechrescom

High-fidelity modeling of dynamic origami folding using Absolute Nodal Coordinate Formulation (ANCF)

Jiayue Tao [b], Ahmed E. Eldeeb [c,d], Suyi Li [a,*]

[a] Department of Mechanical Engineering, Virginia Tech, 1145 Perry St, Blacksburg, 24061, VA, USA
[b] Department of Mechanical Engineering, Clemson University, 216 South Palmetto Blvd., Clemson, 29631, SC, USA
[c] Department of Mechanical and Industrial Engineering, University of Illinois at Chicago, 842 West Taylor Street, Chicago, 60607, IL, USA
[d] Department of Mechanical Design and Production, Faculty of Engineering, Cairo University, Giza, Egypt

ARTICLE INFO

Keywords:
Origami dynamics
Absolute Nodal Coordinate Formulation
High-fidelity modeling

ABSTRACT

Origami has evolved into a framework for creating engineering systems at vastly different scales: from large deployable airframes to architected materials to small DNA machines. These emerging applications require us to develop high-fidelity models that can simulate and examine folding-induced mechanical responses, especially those involving significant facet rotation, non-uniform deformation, and complex dynamics. To this end, this study formulates and experimentally validates a new origami mechanics model based on Absolute Nodal Coordinate Formulation (ANCF), which has unique advantages for predicting the nonlinear dynamics of multibody systems with large rotation and deformation. This new model treats origami facets as ANCF thin plate elements rotating around compliant creases. Moreover, Torsional Spring Damper Actuator (TSDA) connectors are developed to represent crease folding. After careful calibration with experimentally measured constitutive material properties, this study provides the first reported quantitative agreement between simulation predictions and experiment results involving complex and non-uniform facet deformation and transient dynamic responses. Therefore, this model can help deepen our knowledge of folding-induced mechanics and dynamics, fostering future applications for origami.

1. Introduction

Origami – the ancient craftsman art of paper folding – has evolved into a framework for designing and constructing various engineering systems, such as deployable airframes [1–3], multi-functional structures [4–6], architected materials [7,8], soft robots [9,10], medical devices [11,12], and DNA machines [13]. The increasing complexities of these applications require us to thoroughly understand the kinematics, mechanics, and dynamic characteristics of foldable structures and materials [14–16]. To this end, high-fidelity and computationally efficient simulation models are crucial because they can quickly uncover the rich correlations between origami design and the corresponding mechanical properties before time-consuming and labor-expensive experiment efforts.

Over the past decade, many models have been formulated to simulate origami's kinematic motions and mechanical properties. No universal modeling approach exists to address every simulation problem because each model has its scope, advantages, and limitations [1, 17–20]. Moreover, different studies typically aim to achieve widely different simulation objectives. For example, some studies focus on designing for a desired *kinematic motion*, while others target *physical properties*. An obvious example is the popular Freeform Origami model, which allows users to easily design new origami by customizing the vertices locations [21]. It is a powerful tool for kinematics analysis; however, it assumes that the origami facets are rigid panels and creases are like hinges, so this model does not incorporate any constitutive material properties.

A critical development in origami's mechanics and dynamics modeling is the addition of torsional springs to the crease lines. This way, one can estimate the internal bending moments from folding the constitutive sheet materials while continuing to assume rigid facets [22,23]. Such a seemingly simple approach turned out to be surprisingly powerful in revealing the physical principles behind many folding-induced mechanical responses like nonlinear stiffness [24,25], multi-stability [4, 26], and complex dynamics [27,28]. Moreover, if the origami is not rigid-foldable – meaning folding would incur facet deformations – one could add "virtual folds" to segment the deformed facet into a few smaller but rigid parts connected by spring hinges [29,30].

* Corresponding author.
E-mail address: suyili@vt.edu (S. Li).

https://doi.org/10.1016/j.mechrescom.2023.104089
Received 6 November 2022; Received in revised form 18 January 2023; Accepted 3 March 2023
Available online 7 March 2023

The bar-hinge modeling approach is a more complex method to incorporate facet deformations, including in-plane shearing and out-of-plane bending and twisting. This approach places stretchable bar elements along the creases and across facet diagonals, discretizing the continuous origami into a pin-jointed truss frame system. Both linear [6,31] and nonlinear [32,33] versions of bar-hinge models have been developed with many successes in analyzing the global deformation of origami, such as soft modes beyond rigid-folding [34,35] and snap-through response between distant stable equilibria [5,36,37]. The bar-hinge approach is quite versatile: It can be quickly adapted to different origami designs and further expanded for more complex deformations. For example, while the original bar-hinge models still assume the creases behave like hinges with torsional springs, one can analyze more complex crease deformations by adding additional bar elements [38,39], spring elements [40–42], or even plate elements for the creases [43]. Moreover, by assigning discrete point-mass inertia at the vertices, one can advance the bar-hinge model to simulate the dynamic response of folded systems [44–47].

Bar-hinge models are powerful in uncovering the fundamental principles underpinning folding-induced mechanics and dynamic properties. However, they sometimes struggled to provide *quantitatively* accurate predictions compared to physical experiments, especially when transient dynamics and complex facet deformations are involved. To this end, finite element simulation has the advantage. Typically, the origami facets are meshed by shell elements. The creases can be assumed rigid if there is no significant folding [48–53]; otherwise, they can be modeled using spring-hinge elements [7,54,55], or additional shell elements [52,56–59]. However, the disadvantages of finite element simulations are also evident. Building the geometry and executing the simulation can be very time-consuming. More importantly, the traditional shell element might experience convergence issues when large and dynamic rotations occur. This limitation can be constraining because large-amplitude rotations are commonly seen in origami-inspired systems.

Therefore, this paper aims to establish a high-fidelity model capable of accurately predicting the dynamic responses of origamis with complex deformations. To achieve this goal, we adopt the **A**bsolute **N**odal **C**oordinate **F**ormulation (ANCF hereafter). This formulation is widely used to study the nonlinear motions of flexible multibody systems with large displacements and deformation. It uses position and position gradients (aka. slope coordinates) as the nodal coordinates instead of displacements and rotations as in the conventional finite element [60]. Coordinate transformation is not needed in the ANCF because the nodal coordinates are defined in the global coordinate system.

The ANCF approach has several unique advantages for simulating the dynamic responses of origami. First, it applies no assumptions on the rotation and deformation magnitude within the elements [61–65]. It can accurately present the complex and curved facet deformation because it uses position gradients, whereas conventional rotation-based finite element models require more elements to achieve the desired smoothness [66–68]. According to recent investigations, ANCF gives more accurate results than the conventional finite element in the case of soft materials and large deformation [69,70]. Second, ANCF generates constant mass matrices with simple expressions for the inertia forces and without Coriolis/centrifugal forces [61,68], making it computationally efficient to solve origami's dynamic equations of motion. Finally, the continuum mechanics framework adopted by ANCF can account for all geometric non-linearity in the system [61,63,64,71]. Recent developments, advantages, and justifications for using ANCF can be found in these investigations [68,72,73]. These advantages make ANCF an ideal framework to simulate the nonlinear, transient dynamic responses of large origami folding involving complex facet deformations and significant rotations.

This study formulates and validates a new origami dynamics model based on ANCF. This new model describes the origami facets as ANCF thin plate elements rotating around compliant creases, and we developed a new **T**orsional **S**pring **D**amper **A**ctuator (TSDA hereafter) for the overlapping crease nodes between interconnected facets. We validate the new model's accuracy by comparing its prediction to the traditional finite element simulation and experimental results. To the author's best knowledge, this study provides the first reported *quantitative* agreement between simulation predictions and experimental results involving non-uniform and complex facet deformation as well as transient dynamic responses.

In what follows, Section 2 briefly reviews the fundamentals of the ANCF thin plate element and then details the formulation of the new torsional spring damper actuator. Section 3 describes the application of the ANCF framework to origami simulations, with particular attention to crease modeling. Section 4 discusses the accuracy of the ANCF origami model based on two experimental case studies. Finally, Section 5 concludes this paper with a summary and discussion.

2. Fundamentals of absolute nodal coordinate formulation

In continuum mechanics, one can use twelve modes to fully describe an infinitesimal spatial volume: three rigid translations, three rigid rotations, and six deformation modes assigned to the cross-sections [74,75]. In the ANCF approach, the three rigid rotations and the six deformation modes can be described accurately by nine position gradients. These nodal coordinates are sufficient to accurately describe the rigid body motion and the cross-section deformation involving large deformation.

2.1. ANCF thin plate element

Since the origami facets are typically very thin compared to their overall size, we use the gradient-deficient, ANCF thin plate element to model the facets [76]. This element ignores the thickness deformation and eliminates the high-frequency modes. In addition, it can avoid the locking issues that may arise from using fully parameterized ANCF elements for thin structures [62,73,77–79]. As a result, thin plate elements offer better computational efficiency and convergence performance than the fully parameterized ANCF plate elements [76,80].

The global position vector $\mathbf{r}$ of an arbitrary point in the plate's mid-surface is (Fig. 1a):

$$\mathbf{r}(\mathbf{x},t) = \mathbf{S}(\mathbf{x})\mathbf{e}(t), \tag{1}$$

where $\mathbf{S}$ is the element shape function:

$$\mathbf{S}(\mathbf{x}) = \left[s_1\mathbf{I}\ \ s_2\mathbf{I}\ \ s_3\mathbf{I}\ \ s_4\mathbf{I}\ \ s_5\mathbf{I}\ \ s_6\mathbf{I}\ \ s_7\mathbf{I}\ \ s_8\mathbf{I}\ \ s_9\mathbf{I}\ \ s_{10}\mathbf{I}\ \ s_{11}\mathbf{I}\ \ s_{12}\mathbf{I}\right]. \tag{2}$$

Here, $\mathbf{I}$ is the 3×3 identity matrix and the shape functions s_i ($i = 1, 2, 3, \ldots, 12$) are available in the Supplement Materials.

Denote $\mathbf{x} = \begin{bmatrix} x & y \end{bmatrix}^\intercal$ as the spatial coordinates of a point defined in the element coordinate system (note that there is no spatial coordinate z because the deformation of the plate thickness is negligible), one can write the vector of element nodal coordinates $\mathbf{e}$ at node j of any thin-plate element as (Fig. 1a):

$$\mathbf{e}^j = \left[(\mathbf{r}^j)^\intercal \quad (\mathbf{r}_x^j)^\intercal \quad (\mathbf{r}_y^j)^\intercal\right]^\intercal, j = 1, 2, 3, 4, \tag{3}$$

where j is the node number. $\mathbf{r}^j$ represents the global position vector of node j defined in the global coordinate system. The position vector gradients are defined by $\mathbf{r}_x^j = \partial\mathbf{r}^j/\partial x$ and $\mathbf{r}_y^j = \partial\mathbf{r}^j/\partial y$. The third position vector gradient, which differentiates the global position vector with respect to the spatial coordinate z, is not considered in the thin plate element. Therefore, the thin plate element is considered as a gradient-deficient element. Eq. (3) shows that a thin plate element has four nodes, each with nine coordinates, resulting in 36 degrees of freedom.

According to the general continuum mechanics theory, three configurations are necessary to describe the deformation kinematics of the ANCF element: straight configuration $\mathbf{x}$, stress-free (undeformed) reference configuration $\mathbf{X}$, and deformed current configuration $\mathbf{r}$ (Fig. 1b).

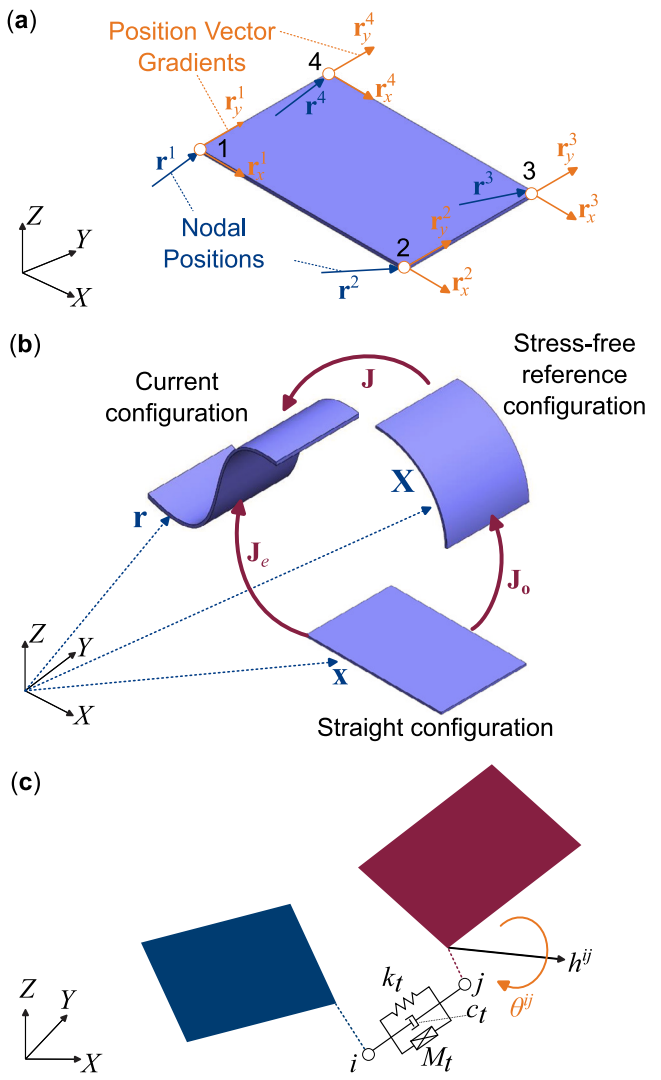

Fig. 1. Fundamentals of ANCF thin plate elements and TSDA connector. (a) Deformation kinematics of a three-dimensional, gradient-deficient ANCF thin plate element, showing its global position coordinate $\mathbf{r}^j$ and its position gradients $\mathbf{r}_x^j$, $\mathbf{r}_y^j$. (b) The three configurations for describing the continuum kinematics of ANCF elements based on the general continuum mechanics theory. (c) The basic setup for a TSDA connector.

Integration and differentiation are carried out in the straight configuration using the matrix of position vector gradient $\mathbf{J}_o = \partial\mathbf{X}/\partial\mathbf{x}$, where $\mathbf{X} = \mathbf{S}\mathbf{e}_o$ and $\mathbf{e}_o$ is the vector of element nodal coordinates in the initial reference configuration. Another matrix of position vector gradient $\mathbf{J}_e = \partial\mathbf{r}/\partial\mathbf{x}$ is used to define the relationship between the current and straight configuration, which leads to $\mathbf{J} = \partial\mathbf{r}/\partial\mathbf{X} = \mathbf{J}_e\mathbf{J}_o^{-1}$ [81].

Since the ANCF thin plate element does not consider the z−direction position gradient, its matrices of position vector gradient $\mathbf{J}_o$ and $\mathbf{J}_e$ are not square. Therefore, one needs to add a unit vector normal to the mid-surface. For example, one can add the unit normal vector $\mathbf{k}_m = (\mathbf{r}_x \times \mathbf{r}_y)/|\mathbf{r}_x \times \mathbf{r}_y|$ to $\mathbf{J}_e$ (the subscript m denotes the mid-surface) so that $\mathbf{J}_e = \begin{bmatrix}\mathbf{r}_x & \mathbf{r}_y & \mathbf{k}_m\end{bmatrix}$. Note that this normal vector is not a position vector gradient; it is introduced only to generate square matrices for subsequent numerical calculations. The nonlinear Green–Lagrange strain tensor $\boldsymbol{\epsilon}_m$, which ensures zero strain in the initial reference configuration, can be written in terms of the matrix of position vector gradient $\mathbf{J}$ in the following form:

$$\boldsymbol{\epsilon}_m = \frac{1}{2}\left(\mathbf{J}^{\intercal}\mathbf{J} - \mathbf{I}\right) = \frac{1}{2}\left(\mathbf{J}_o^{-\intercal}\mathbf{J}_e^{\intercal}\mathbf{J}_e\mathbf{J}_o^{-1} - \mathbf{I}\right). \tag{4}$$

The strain components associated with the unit vectors can be easily found as 0, that is, $\epsilon_{m13} = \epsilon_{m23} = \epsilon_{m33} = 0$. It also implies that the plate has a constant thickness. This Green–Lagrange strain tensor based on the continuum mechanics approach accounts for all geometric non-linearity [61,63,64,71].

The equation of motion of the ANCF elements is:

$$\mathbf{M}\ddot{\mathbf{e}} = \mathbf{Q}_s + \mathbf{Q}_e. \tag{5}$$

The constant mass matrix $\mathbf{M}$ can be written as $\mathbf{M} = \int_{V_o} \rho\mathbf{S}^{\intercal}\mathbf{S}\mathrm{d}V_o$, where ρ and V_o are the element mass density and volume in the initial reference configuration, respectively. Since the integration should be calculated in the straight configuration, one can substitute the relationship between initial reference configuration and straight configuration using $\mathbf{J}_o$ and rewrite the infinitesimal volume as $\mathrm{d}V_o = |\mathbf{J}_o|\mathrm{d}V$, where V is the element volume in the straight configuration.

The generalized elastic forces vector $\mathbf{Q}_s$ in Eq. (5) is evaluated in the current configuration with respect to the stress-free reference configuration, which can be a complex curved geometry as shown in Fig. 1(b). Therefore, the strain energy of ANCF thin plate elements can be written as [76,81]:

$$U = \frac{1}{2}\int_V \boldsymbol{\epsilon}^{\intercal}\mathbf{E}_{\epsilon}\boldsymbol{\epsilon}|\mathbf{J}_o|\mathrm{d}V + \frac{1}{2}\int_V \boldsymbol{\kappa}^{\intercal}\mathbf{E}_{\kappa}\boldsymbol{\kappa}|\mathbf{J}_o|\mathrm{d}V, \tag{6}$$

where the matrices of elastic coefficients in Eq. (6) are:

$$\mathbf{E}_{\epsilon} = \frac{E}{1-\nu^2}\begin{bmatrix}1 & \nu & 0\\ \nu & 1 & 0\\ 0 & 0 & \frac{1-\nu}{2}\end{bmatrix},\ \mathbf{E}_{\kappa} = \frac{t^2}{12}\mathbf{E}_{\epsilon}. \tag{7}$$

E is the constitutive material's elastic modulus, ν is the Poisson's ratio, and t is the plate thickness. $\boldsymbol{\epsilon}$ is the strain vector at the plate mid-surface. Based on the Green–Lagrange strain tensor $\boldsymbol{\epsilon}_m$ in Eq. (4), one can have $\boldsymbol{\epsilon} = \begin{bmatrix}\epsilon_{m11} & \epsilon_{m22} & 2\epsilon_{m12}\end{bmatrix}^{\intercal} = \begin{bmatrix}\epsilon_{xx} & \epsilon_{yy} & 2\epsilon_{xy}\end{bmatrix}^{\intercal}$. Here ϵ_{xx}, ϵ_{yy} and ϵ_{xy} are the normal axial, normal transverse, and shear strains, respectively. The curvature vector $\boldsymbol{\kappa}$ can be obtained as $\boldsymbol{\kappa} = \begin{bmatrix}\kappa_{xx} & \kappa_{yy} & 2\kappa_{xy}\end{bmatrix}^{\intercal}$, where the curvature components are calculated in terms of the position vector gradients:

$$\kappa_{xx} = \frac{\mathbf{r}_{xx}^{\intercal}\mathbf{n}}{\|\mathbf{n}\|^3}, \kappa_{yy} = \frac{\mathbf{r}_{yy}^{\intercal}\mathbf{n}}{\|\mathbf{n}\|^3}, \kappa_{xy} = \frac{\mathbf{r}_{xy}^{\intercal}\mathbf{n}}{\|\mathbf{n}\|^3}. \tag{8}$$

Here, $\mathbf{n} = \mathbf{r}_x \times \mathbf{r}_y$ is the normal vector to plate mid-surface. Finally, the vector of generalized elastic forces $\mathbf{Q}_s$ can be calculated by differentiating the strain energy U with respect to the vector of element nodal coordinates $\mathbf{e}$ so that:

$$Q_s = -\frac{\partial U}{\partial \mathbf{e}} = -\int_V \left(\frac{\partial \boldsymbol{\epsilon}}{\partial \mathbf{e}}\right)^{\intercal}\mathbf{E}_{\epsilon}\boldsymbol{\epsilon}|\mathbf{J}_o|\mathrm{d}V - \int_V \left(\frac{\partial \boldsymbol{\kappa}}{\partial \mathbf{e}}\right)^{\intercal}\mathbf{E}_{\kappa}\boldsymbol{\kappa}|\mathbf{J}_o|\mathrm{d}V. \tag{9}$$

$\mathbf{Q}_e$ in Eq. (5) represents the vector of generalized external forces. In this study, it originates from the compliant crease as we detail in the following sub-section.

2.2. Torsional spring damper actuator

In the new origami model, we assign torsional springs to the overlapping nodes along the origami creases. Equivalently, one can apply external Cartesian moments to these crease nodes. These external moments are formulated in the ANCF framework using the torsional spring damper actuators (TSDA). Considering a TSDA connector that connects two facets at two nodes i and j as shown in Fig. 1(c). This connector has a torsional spring coefficient k_t, a torsional damping coefficient c_t, and an actuator moment M_t. The total exerted moment becomes:

$$M = k_t\left(\theta^{ij} - \theta_o^{ij}\right) + c_t\dot{\theta}^{ij} + M_t, \tag{10}$$

where θ^{ij}, θ_o^{ij}, and $\dot{\theta}^{ij}$ are the relative angular displacement, the corresponding undeformed angular displacement, and relative angular velocity between nodes i and j, respectively. The virtual work of the external moment M is $\delta W = \mathbf{M}^{\intercal}\delta\boldsymbol{\pi}$, where $\mathbf{M} = M\mathbf{h}^{ij}$ is the external Cartesian moment vector, and $\mathbf{h}^{ij}$ is a unit vector along the axis of

rotation (Fig. 1c). The virtual angular rotation vector $\delta\boldsymbol{\pi}$ can be related to the virtual change of the element nodal coordinates $\delta\mathbf{e}$ so that $\delta\boldsymbol{\pi} = \mathbf{G}\delta\mathbf{e}$. Here, the matrix $\mathbf{G}$ is used to obtain the generalized forces, associated with the element nodal coordinates, due to applied Cartesian moment:

$$\mathbf{G} = \frac{1}{2}\left(\sum_{m=1}^{3}\mathbf{J}_m^{-1}\times\frac{\partial\mathbf{r}_m}{\partial\mathbf{e}}\right), \tag{11}$$

where $\mathbf{J}_m^{-1}$ is the mth row of the inverse of position vector gradient matrix, and $\mathbf{r}_m$ is the position vector gradient, where $\mathbf{r}_1 = \mathbf{r}_x$, $\mathbf{r}_2 = \mathbf{r}_y$ and $\mathbf{r}_3 = \mathbf{r}_z$ [82]. Therefore, the virtual work due to the TSDA connector can be written in terms of the virtual change of the vector of the element nodal coordinates in that:

$$\delta W = \mathbf{Q}_e^{iT}\delta\mathbf{e}^i + \mathbf{Q}_e^{jT}\delta\mathbf{e}^j. \tag{12}$$

$\mathbf{Q}_e^i = -\mathbf{G}^{iT}\mathbf{M}$ and $\mathbf{Q}_e^j = \mathbf{G}^{jT}\mathbf{M}$ are the vector of generalized external moments associated with the element nodal coordinates at nodes i and j, respectively. To simulate the motion of a multi-body system with torsional spring constraints, one can apply the TSDA connectors in the ANCF framework and introduce the assembled vector of generalized external moments into Eq. (5).

Another important parameter to calculate is the relative angular displacement θ^{ij}. It is determined based on the relative transformation matrix between the two nodes i and j. At node i, we assume the X^i axis of its orthogonal element coordinates system is $\hat{\mathbf{r}}_x^i$ so that $\mathbf{v}_1^i = \hat{\mathbf{r}}_x^i = \mathbf{r}_x^i/|\mathbf{r}_x^i|$. Since the position gradients $\mathbf{r}_x$ and $\mathbf{r}_y$ are linearly independent, the Z^i axis can be obtained from a cross-product $\mathbf{v}_3^i = (\hat{\mathbf{r}}_x^i\times\hat{\mathbf{r}}_y^i)/|\hat{\mathbf{r}}_x^i\times\hat{\mathbf{r}}_y^i|$. The Y^i axis is determined by the cross product of the unit vectors $\mathbf{v}_3^i$ and $\mathbf{v}_1^i$ so that $\mathbf{v}_2^i = \mathbf{v}_3^i\times\mathbf{v}_1^i$. Therefore, the transformation matrix at the first node i is written as $\mathbf{A}^i = \begin{bmatrix}\mathbf{v}_1^i & \mathbf{v}_2^i & \mathbf{v}_3^i\end{bmatrix}$. Using the same procedure, the transformation matrix of the second node j is determined as $\mathbf{A}^j = \begin{bmatrix}\mathbf{v}_1^j & \mathbf{v}_2^j & \mathbf{v}_3^j\end{bmatrix}$. The relative transformation matrix $\mathbf{A}^{ij}$ between the two nodes is evaluated using $\mathbf{A}^{ij} = \mathbf{A}^{jT}\mathbf{A}^i$. Knowing the relative transformation matrix $\mathbf{A}^{ij}$, one can obtain the relative angular displacement θ^{ij} and the axis of rotation using the Rodriguez formula such that [83]

$$\theta^{ij} = cos^{-1}\left(\frac{a_{11}+a_{22}+a_{33}-1}{2}\right),\quad \mathbf{h}^{ij} = \frac{1}{2\sin\theta^{ij}}\begin{bmatrix}a_{32}-a_{23}\\ a_{13}-a_{31}\\ a_{21}-a_{12}\end{bmatrix}, \tag{13}$$

where a_{lk} $(l,k = 1,2,3)$ are the components of the transformation matrix $\mathbf{A}^{ij}$. It should be mentioned that the axis of rotation is defined in the body in which relative orientation is defined: θ^{ij} represents the rotation angle with respect to node j, so the unit vector of the axis of rotation $\mathbf{h}^{ij}$ should be defined at j (Fig. 1c).

It is worth noting that the angular displacement formulation here is generic and applies to many different structures. In the following Section 3, we will re-iterate the formulation specifically for origami.

2.3. Validating the TSDA formulation

Before implementing the ANCF to analyze origami dynamics, we first validate the TSDA formulation by comparing its results to traditional finite element simulations. To this end, we use two examples: one is a simple rigid pendulum, and the other is a soft plate pendulum. In these two examples, we obtain ANCF results by using the general-purpose MBS software **SIGMA/SAMS** (**S**ystematic **I**ntegration of **G**eometric **M**odeling and **A**nalysis for the **S**imulation of **A**rticulated **M**echanical **S**ystems), while the finite element package is Abaqus.

Simple Rigid Pendulum: In the first validation example, a simple rigid pendulum is connected to the ground via a TSDA element with $k_t = 1000$ N m/rad. It rotates around the global Z-axis under its gravity. Fig. 2(a) summarizes the vertical displacement predictions of the pendulum tip (point P) from Sigma/Sams, Abaqus, and the analytical solution, respectively. The ANCF model with TSDA agrees precisely with the conventional finite element simulation and analytical prediction.

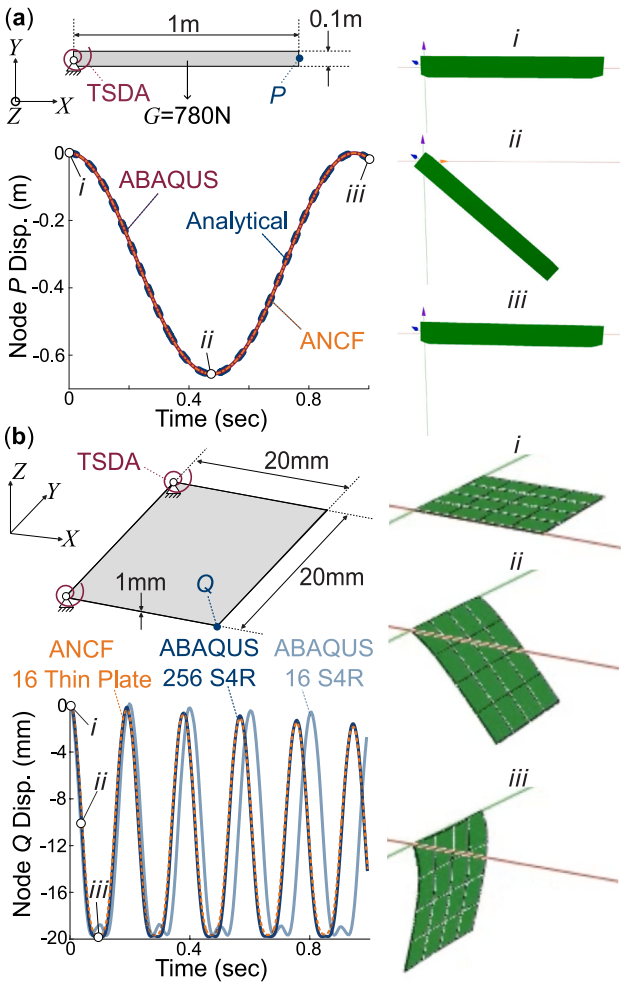

Fig. 2. Validation of TSDA formulation. (a) The kinematic setup and simulation results of a simple, rigid pendulum based on different methods. The results show precise agreement. The figures on the right illustrated the ANCF-simulated deformation of the pendulum at different time instants. (b) The simulated results of a soft plate pendulum.

Soft Plate Pendulum: While the first validation example only uses a TSDA connector, the second example involves integrating TSDA with the thin plate elements in the ANCF framework. In this example, a square-shaped soft plate is connected to the ground by two torsional spring damper actuators at its corners (Fig. 2b). The localized torsional spring coefficient, defined in Eq. (10), is $k_t = 0.1$ N mm/rad and the localized damping coefficient is $c_t = 0.001$ N mm s/rad. The soft plate pendulum made of silicone rubber material has Young's modulus $E = 1$ MPa, Poisson's ratio $\nu = 0.47$, thickness 1 mm. The soft pendulum is initially undeformed and held flat in the horizontal $X-Y$ reference plane, then falls freely under its gravity. Fig. 2(b) summarizes the simulation results from Sigma/Sams using 16 ANCF thin-plate elements, as well as two simulations from Abaqus using 16 or 256 conventional shell elements (S4R). We use the S4R element as the benchmark here because it is a robust, general-purpose element suitable for various shell structure modeling tasks. Indeed, many published finite element studies on origami (reviewed in the introduction section) used S4R. Here, ANCF converges with Abaqus precisely again, validating the correctness of the TSDA formulation. Moreover, this example elucidates an important advantage of ANCF: It requires fewer elements to simulate complex dynamics than conventional finite elements. In this example, ANCF converges with 16 (= 4×4) elements with 576 degrees of freedom

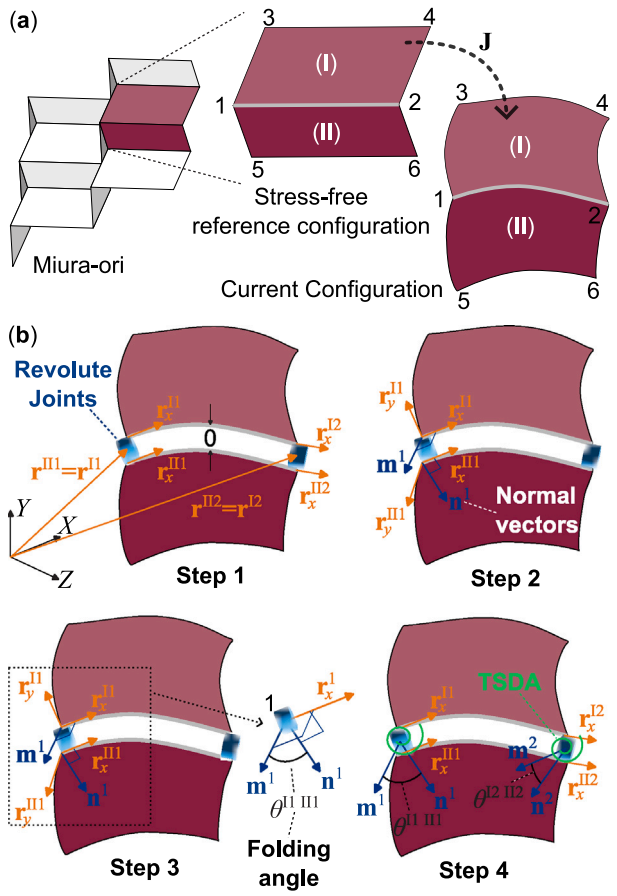

Fig. 3. Applying ANCF framework and TSDA connector to origami. (a) This illustration focuses on two adjacent facets from the classical Miura-ori. Since we assume the Miura-ori is soft, its facets and creases can show bending or twisting in addition to folding, leading to a curve-shaped crease at the current configuration. (b) The four consecutive steps for modeling the origami crease: (1) applying revolute joints; (2) calculating normal vectors; (3) obtaining folding angle; and (4) adding TSDA connectors.

(nodal coordinates) in total, while Abaqus requires 256 elements with 6144 degrees of freedom (Fig. 2(b)).

3. Implementing TSDA to origami

In principle, origami deformation involves thin and soft surfaces (facets) rotating about compliant creases. Accordingly, one can mesh the origami facets using the ANCF thin-plate elements and model the crease lines by applying TSDA connectors at the overlapping nodes between adjacent facets. This approach applies to either straight or curved creases at different deformation configurations.

To elucidate the modeling approach, we use two adjacent facets in a soft Miura-ori sheet as an example (Fig. 3a). For simplicity, we assume each facet is meshed by only one thin-plate element: Element (I) with nodes 1-2-4-3 and element (II) with nodes 5-6-2-1. These two elements connect at the two nodes 1 and 2 at the two ends of the crease line. Certainly, one can apply a more refined mesh with more nodes along the crease for higher accuracy, but the underlying modeling approach stays the same.

Fig. 3(b) details the four consecutive steps for modeling origami crease under the ANCF framework. In step 1, one connects the two thin plates by revolute joints at the crease node 1 and 2, respectively. These revolute joints require that the two plates share the same position at the two crease nodes and that the two position gradients along the crease line are equal:

$$\mathbf{r}^{\mathrm{I}j} = \mathbf{r}^{\mathrm{II}j} \text{ and } \mathbf{r}_x^{\mathrm{I}j} = \mathbf{r}_x^{\mathrm{II}j},\ j = 1,2. \tag{14}$$

Here, the superscript Ij and IIj ($j = 1,2$) represent the crease nodes on the two thin-plate facet elements (I) and (II), respectively. In this way, the revolute joint's rotational axis lies along the position gradient vector in the localized x-axis ($\mathbf{r}_x^{\mathrm{I}j}$ or $\mathbf{r}_x^{\mathrm{II}j}$, $j = 1,2$). In other words, the rotational axis remains tangent to the crease line at the current configuration.

In step 2, one can calculate the folding angle (or angular displacement) between the two facets at the revolute joints. Since the nodal coordinates in ANCF are the position gradients, defining these rotational angles is not trivial. To this end, we introduce local vectors $\boldsymbol{m}^j$ for facet I at nodes j:

$$\boldsymbol{m}^j = \left(\mathbf{r}_x^{\mathrm{I}j} \times \mathbf{r}_y^{\mathrm{I}j}\right) \times \mathbf{r}_x^{\mathrm{I}j},\ j = 1,2. \tag{15}$$

These vectors are always perpendicular to the rotational axis ($\boldsymbol{m}^j \perp \mathbf{r}_x^{\mathrm{I}j}$). Similarly, we introduce local vectors $\boldsymbol{n}^j$ for another facet II at the same nodes, which satisfies $\boldsymbol{n}^j \perp \mathbf{r}_x^{\mathrm{II}j}$:

$$\boldsymbol{n}^j = \left(\mathbf{r}_x^{\mathrm{II}j} \times \mathbf{r}_y^{\mathrm{II}j}\right) \times \mathbf{r}_x^{\mathrm{II}j},\ j = 1,2. \tag{16}$$

Here, the operator "×" denotes cross-product. In step 3, one can calculate the rotational angle between the two facets at node j based on these normal vectors so that:

$$\theta^{\mathrm{I}j\ \mathrm{II}j} = \cos^{-1}\left(\frac{\boldsymbol{m}^j \cdot \boldsymbol{n}^j}{\|\boldsymbol{m}^j\|\|\boldsymbol{n}^j\|}\right) \bmod 2\pi,\ j{=}1{,}2, \tag{17}$$

where the symbol "mod" means modulo operation. Note that this equation is equivalent to the angular displacement Eq. (13), but written specifically for origami. Finally in step 4, one can add the torsional spring damper actuator TSDA element at crease nodes to simulate origami folding based on Eq. (10).

4. Case studies

In this section, we assess the accuracy of the proposed ANCF model by comparing its predictions to experiments with transient dynamic responses of origami. Two case studies are conducted: One uses a simple accordion fold, and the other uses the classical Miura-ori pattern.

4.1. Measuring the constitutive material properties

We fold the origami test samples using 0.127 mm thin Polyethylene terephthalate (PET) sheets. It has a material density of 1384 kg/m^3. To conduct the ANCF simulation, one needs to provide the elastic modulus E, Poisson's ratio ν, and the equivalent torsional stiffness of the origami crease k_t. To measure E, we cut dogbone samples according to the ASTM-D638 standard and then measure their stress–strain relationship on a universal tester machine (ADMET eXpert 5600 with 3D-printed gripper, Fig. 4a). To estimate the Poisson's ratio, we further attach two pairs of green markers within the gage length of the dogbone specimens (Fig. 4a): one pair (H_1, H_2) is used to measure the horizontal deformation, while the other pair (V_1, V_2) is for vertical deformation. We capture high-resolution videos of the specimen during tensile tests and use MATLAB's video processing tools to extract the marker center's displacements.

Fig. 4(b) summarizes the stress–strain curves obtained from 7 test specimens, exhibiting a consistent elastic behavior before yielding. The Young's modulus E of the PET sheet, calculated from the initial linear portion of the stress–strain curves, is 7.09 ± 0.02 GPa.

Poisson's ratio ν can be obtained from the marker's displacements. Fig. 4(c) shows an example of the horizontal and vertical displacements of the two marker pairs. From these displacements, one can calculate the vertical strain $\epsilon_L = (L - L_o)/L_o$ and transverse strain $\epsilon_T = (W - W_o)/W_o$. The averaged Poisson's ratio of PET sheet, obtained from the ratio of these two strains $\nu = -\epsilon_T/\epsilon_L$, is 0.187. Many factors, such as fabrication method, testing temperature, and material composition, can influence Poisson's ratio and Young's modulus. So we ensure the material selection and experiment condition of the PET property tests

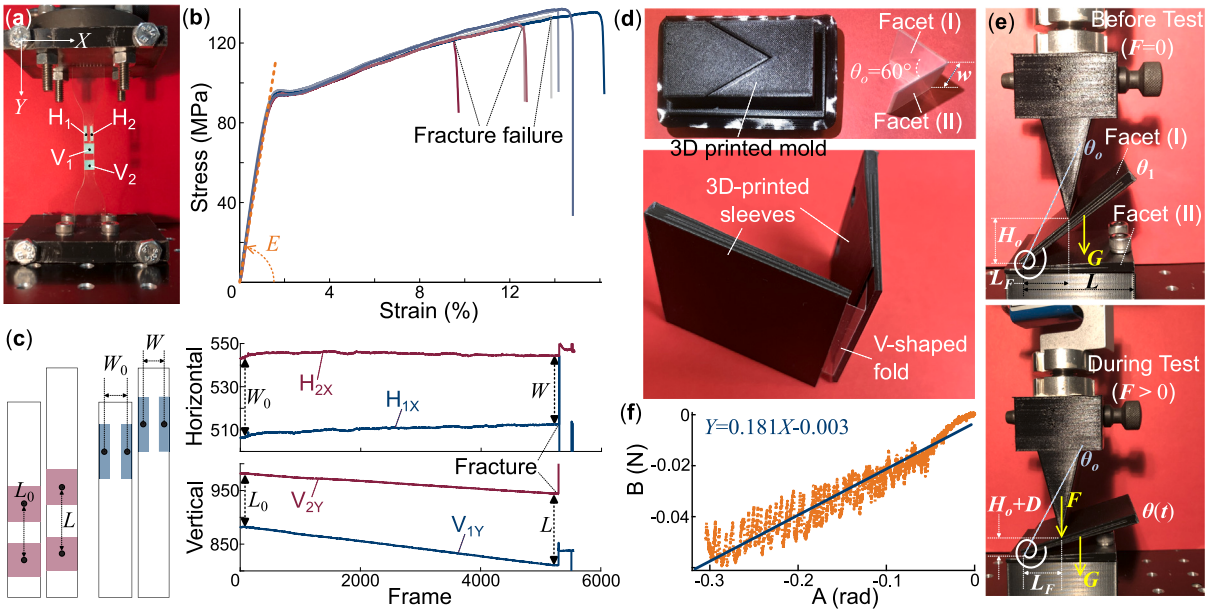

Fig. 4. Measuring the constitutive material properties of PET sheets and PET-based origami folds. (a) Tensile test setup of PET dogbone samples with attached markers. (b) Measured stress–strain relationships of 7 dogbone samples, showing consistent results before yielding. (c) Relative horizontal and vertical displacement measurements between the two pairs of markers on the dogbone. We use these displacements to calculate Poisson's ratio. For clarity, only one sample data is shown here. (d) A V-shaped origami sample from 3D printed mode. Then another set of 3D-printed sleeves are added to reinforce the facets so the sample would deform only by crease folding in the subsequent tests. (e) Experiment set up for measuring the reaction moment from folding (bending) the origami crease. Here, the sample's deformations before and during the test are shown. (f) The calculated responses from crease folding.

match the subsequent origami case study experiment as closely as possible.

To measure the crease's torsional stiffness k_t, we fold a small PET sheet into a V-shaped sample with one crease line, constrain it in a 3D-printed mold, then anneal it at 150 °F for 30 min (Fig. 4d). The purpose of such annealing is to relieve the residual stress from the plastic material deformation due to folding and maintain a consistent initial folding angle ($\theta_o = 60°$ in our tests). Then we design and 3D print stiff "sleeves" to cover the two facets of the V-shaped sample and then place the assembly on the universal tester machine to measure the reaction force from bending (or folding) the crease (Fig. 4e). These stiff sleeves ensure the sample deforms only by crease folding without any facet deformations. The displacement rate in these tests is $V_d = -0.1$ mm/s, and six samples are tested.

Since we assume origami creases behave like hinges with linear torsional springs [34,41,84], its resistant moment against quasi-static folding, according to Eq. (10), can be simplified to:

$$M = k_t\left(\theta - \theta_o\right) = kw\left(\theta - \theta_o\right) \tag{18}$$

where k is the torsional stiffness coefficient *per unit length* along the crease, and w is the crease's width at undeformed configuration. θ_o is the stress-free folding angle. In these tests, the V-shaped sample is placed horizontally, so its crease deforms due to its upper facet's weight before the tester machine applies any external force. A simple moment balance analysis at the crease's rotation axis gives the following relationship (Fig. 4e):

$$kw(\theta_1 - \theta_o) + G\frac{L}{2}\cos\theta_1 = 0 \tag{19}$$

where G is the weight of the upper facet (I) and its sleeve, L is the facet's length, and θ_1 is the folding angle at the beginning of the test, which can be obtained by $\theta_1 = \tan^{-1}(H_o/L_F)$ according to Fig. 4e.

After the external force is applied to the V-shaped sample, the moment balance equation becomes

$$kw\left(\theta(t) - \theta_o\right) + G\frac{L}{2}\cos\theta(t) - F(t)L_F = 0 \tag{20}$$

Here, $\theta(t)$ is the crease's folding angle at the current configuration. $\theta(t) = \tan^{-1}((H_o + D(t))/L_F)$, where $D(t)$ is the tester overhead's displacement, $F(t)$ is the applied force, and L_F is the corresponding bending moment's arm length. Note that we neglect the inertial effects in this case due to the low displacement rate.

Substituting Eq. (19) into Eq. (20), and introducing Taylor Expansion in that $\cos\theta(t) = 1 - \theta^2(t)/2! + \theta^4(t)/4! + O(\theta^6(t))$, on can obtain

$$\frac{F(t)L_F b}{w} \approx k\left[-\frac{1}{24}a\theta^4(t) + \frac{1}{2}a\theta^2(t) + b\theta(t) - \left(b\theta_o + a\right)\right] \tag{21}$$

Here, the constants $a = \theta_1 - \theta_o$, and $b = \cos\theta_1$. One can re-write this equation as a linear function $B = kA$, where $B = F(t)L_F b/w$ and $A = -a\theta^4(t)/24 + a\theta^2(t)/2 + b\theta(t) - (b\theta_o + a)$. Finally, the averaged torsional spring stiffness *per unit length*, obtained by linear regression of measured $B - A$ curves, is $k = 0.188 \pm 0.037$ N/rad (Fig. 4f).

4.2. Case study 1: Simple fold origami

The first case study examines the transient dynamic response of a PET-based, simple fold origami sample consisting of two rectangular facets connected by a straight crease line. This study involves all the critical components of a complex folding motion, including facet and crease deformations, inertia effects, and damping, but the origami geometry is relatively straightforward. Therefore, it is ideal for validating the accuracy of the proposed ANCF origami model.

The fabrication process of the origami sample is the same as the V-shaped sample discussed in the previous section. The initial stress-free folding angle $\theta_o = 60°$ and other design parameters are summarized in Table 1. Fig. 5(a) shows the experimental set-up at the beginning of the experiment ($t = 0$). The simple fold origami sample is fixed at its top end, and a 5.43-gram payload mass is attached to the free end. We use a fishing line to hold the origami at its initial stress-free configuration. Immediately after the fishing line is cut, the origami would stretch and rebound due to the payload weight, exhibiting an oscillatory motion. Essentially, the simple fold origami behaves like a damped spring. We use a high-speed camera (Kron Technology Chronos 2.1) and MATLAB's video processing tools to extract origami's end displacement (labeled by a green marker).

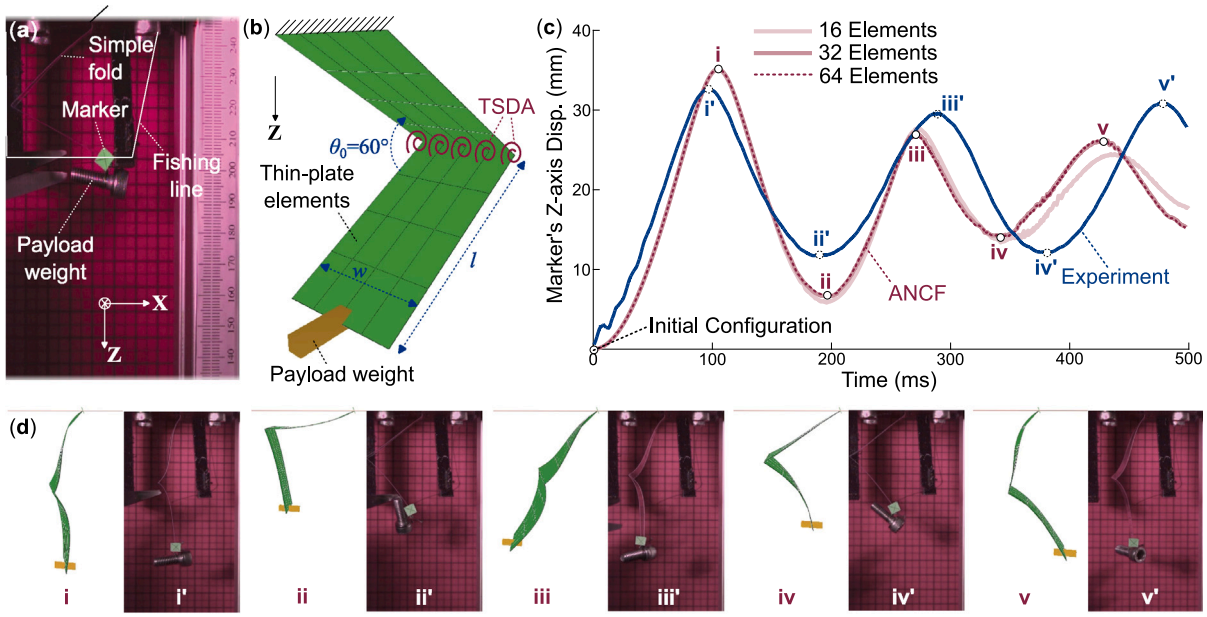

Fig. 5. Case study on the transient dynamic motion of a simple-folded origami due to payload weight. (a) The experimental set-up before the fishing line is cut. (b) The corresponding ANCF model using five TSDA connectors at the crease. Note that the ANCF thin plate elements are fully fixed at the top. (c) Comparison between the ANCF model's prediction and experimental result regarding the marker's vertical displacement along the Z-axis. (d) Comparison of predicted simple fold deformation and experimental images at different time instances.

Fig. 5(b) shows a corresponding ANCF model setup: In this case, each facet is meshed by 16(=4 × 4) thin-plate elements, and TSDA connectors are assigned at every crease node. According to the previous section's results, the origami crease's total torsional spring coefficient is $k \times w = 3.76$ N mm/rad, where k is the measured torsional spring coefficient per unit length. Therefore, one can evenly distribute the total spring coefficient to the five crease nodes so that $k_t = \frac{1}{5}kw = 0.752$ N mm/rad for every TSDA connector. In addition, we estimate the damping coefficient is 2×10^{-5} N mm s/rad at each node. If a finer or coarser mesh is used, each TSDA connector will receive a different share of spring and damping coefficients accordingly.

Fig. 5(c) shows the ANCF model's simulation results based on different mesh densities and the experiment data. More detailed comparisons regarding the origami's external shape at different time instants are available in Fig. 5(d) and supplementary video. The advantage of the ANCF model is evident in this case study, where only 32 elements are required to achieve convergence (that is, further increasing the ANCF element number to 64 does not change the simulation output). Moreover, the converged ANCF model predictions agree *quantitatively* with the experiment data. The ANCF's simulation shows a slightly bigger damping. One could address this discrepancy with a more comprehensive study on the structural damping of origamis. However, it is beyond the scope of this paper.

4.3. Case study 2: Miura-ori

The second case study examines the dynamic deployment (or unfolding) of a PET-based Miura-ori sample under a payload weight. The Miura-ori sample used in this study consists of 4 (= 2 × 2) unit cells, and its geometric designs are summarized in Table 1. The fabrication process is similar to the simple-fold sample, and its initial stress-free folding angle is set to $\theta_o = 80°$ after annealing. Fig. 6(a) shows the experimental setup at the beginning. A 40.56-gram payload mass is attached at the lower left corner. We again use a fishing line to hold the Miura-ori sample at its initial stress-free configuration, and it deploys immediately after cutting the fishing line, showing a dynamic deployment motion. It is worth noting that because the payload weight is at the side and the plastic-based origami is soft, the Miura-ori sample's dynamic deformation becomes far more complex than its rigid-folding kinematics, showing non-uniform facet bending and twisting in addition to crease folding.

Table 1
System parameters for the simple fold origami and Miura-ori case studies.

Constitutive material properties			
E	7.09 GPa	ν	0.187
k	0.188 N/rad	t	0.127 mm
Simple fold design parameters			
l	40 mm	w	20 mm
θ_o	60°		
Miura-ori design parameters			
a	20 mm	b	20 mm
γ	60°	θ_0	80°

Fig. 6(b) shows the corresponding ANCF model setup. The facets in each unit cell are meshed by ANCF thin-plate elements with TSDA connectors assigned at every crease node. At the vertices where four crease lines meet (highlighted in Fig. 6b), we assign four TSDA connectors between every two interconnected facets. The Miura-ori connects to the ground via two pin joints at point A and B, respectively, and only rotation around the pin axis is allowed. The torsional spring and damping coefficients distribution follows the same rule as in the previous case studies.

Fig. 6(c) compares the experimental measured vertical displacement of the marker to the ANCF model's simulation based on different mesh densities. It shows that 144 elements are required to achieve convergence because further increasing the element number to 256 does not change the simulation output. Detailed comparisons of the Miura-ori dynamic deformation are shown in Fig. 5(d) and supplementary video. One can see that ANCF successfully captures the transient and non-uniform dynamic deformation with reasonable accuracy. To the authors' best knowledge, this is the first reported numerical simulation

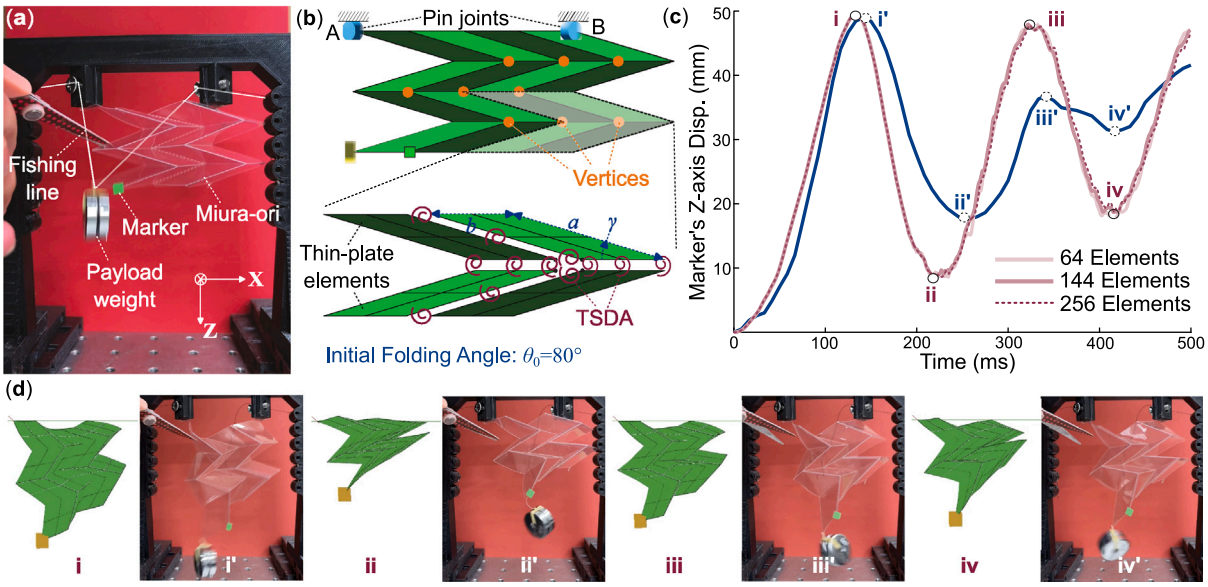

Fig. 6. Case study on the transient and non-uniform dynamic deformation of a Miura-ori sample due to payload weight. (a) The experimental set-up before the fishing line is cut. (b) The corresponding ANCF model. Note that 4 TSDAs are used at every vertex to represent the four crease lines that join at this location. (c) Comparison between the ANCF model's prediction and experimental result regarding the marker's vertical displacement along the Z-axis. (d) Comparison of predicted Miura-ori deformation and experimental images at different time instances.

result that *quantitatively* agrees with the experiment involving complex and transient dynamic responses in origami.

There are also notable discrepancies between the ANCF predictions and experiment results, especially regarding damping. The Miura-ori sample shows more damping than the ANCF simulations, and the difference is more significant compared to the simple fold case. This discrepancy might result from concentrated plastic material deformation near the vertices. Because the vertices have a very complex shape, with three mountain creases and one valley crease joining, they can exhibit enough stress concentration that can influence the overall response of the Miura-ori [85]. Another source of discrepancy is the rigid body rotation of the payload mass, which is evident in the experiment results but not considered in the simulation. Regardless, the two case studies validate the proposed ANCF origami model for its capability to simulate soft origami's transient and complex dynamic responses.

5. Conclusions and discussions

This study formulates and validates a new numerical modeling approach – based on the **A**bsolute **N**odal **C**oordinate **F**ormulation (ANCF) – that can predict origami's complex dynamic deformations with quantitative accuracy. This model describes origami facets as ANCF thin plate elements rotating around compliant creases. To accurately estimate the crease folding, we create a **T**orsional **S**pring **D**amper **A**ctuator (TSDA) to connect the overlapping crease nodes between adjacent facets. We detail the formulation of the TSDA connector and validate it by comparing its prediction to commercial finite element simulation. Finally, we experimentally assess the new model's accuracy based on two case studies involving transient and non-uniform dynamic deployment (or folding) of simple fold origami and Miura-ori structures.

The simulation results from the new ANCF model can predict dynamic responses of origamis with quantitative accuracy. To the author's best knowledge, this is the first reported analysis of origami – involving transient dynamics and complex facet deformations – that shows quantitative agreement between numerical simulation and experiment. Based on the new model, one can simulate origami's dynamics with complex patterns and curved facet deformations using fewer elements than traditional finite element methods. Besides, the ANCF origami model can capture large rotations of origami facets because it applies no assumptions on the rotation and deformation magnitude within the elements. Meanwhile, it can account for all geometric non-linearity of origami due to its foundation in the general continuum mechanics theory. Therefore, this study's results elucidate a significant advancement in the theoretical modeling for the mechanics and dynamics of origami.

Declaration of competing interest

The authors declare the following financial interests/personal relationships which may be considered as potential competing interests: Suyi Li reports financial support was provided by National Science Foundation. Jiayue Tao reports financial support was provided by National Science Foundation.

Data availability

Data will be made available on request.

Acknowledgments

Tao, J. and Li, S. acknowledge the support from National Science Foundation, United States (CMMI-1751449 CAREER). All authors sincerely thank Dr. Ahmed A. Shabana at the University of Illinois, Chicago, United States for fruitful discussions and academic advice. The authors also acknowledge the support from the University of Illinois, Chicago, United States for providing computation resources.

Appendix A. Supplementary data

1. ANCF element's shape function

The shape functions of the thin plate element in Eq. (2) are given by [81]

$$s_1 = -(\xi-1)(\eta-1)(2\eta^2-\eta+2\xi^2-\xi-1),$$
$$s_2 = -a\xi(\xi-1)^2(\eta-1),\ s_3 = -b\eta(\eta-1)^2(\xi-1),$$
$$s_4 = \xi(2\eta^2-\eta-3\xi+2\xi^2)(\eta-1),\ s_5 = -a\xi^2(\xi-1)(\eta-1),$$
$$s_6 = b\xi\eta(\eta-1)^2,\ s_7 = -\xi\eta(1-3\xi-3\eta+2\eta^2+2\xi^2),\ s_8 = a\xi^2\eta(\xi-1),$$
$$s_9 = b\xi\eta^2(\eta-1),\ s_{10} = \eta(\xi-1)(2\xi^2-\xi-3\eta+2\eta^2),$$
$$s_{11} = a\xi\eta(\xi-1)^2,\ s_{12} = -b\eta^2(\xi-1)(\eta-1),$$

where $\xi = x/a$ and $\eta = y/b$. a and b are the plate's length in x and y directions respectively.

2. Video of the dynamic deformation of simple fold and Miura-ori

Supplementary material related to this article can be found online at https://doi.org/10.1016/j.mechrescom.2023.104089.

References

[1] S. Li, H. Fang, S. Sadeghi, P. Bhovad, K.W. Wang, Architected Origami materials: How folding creates sophisticated mechanical properties, Adv. Mater. 31 (2019) 1–18, http://dx.doi.org/10.1002/adma.201805282.

[2] S.A. Zirbel, R.J. Lang, M.W. Thomson, D.A. Sigel, P.E. Walkemeyer, B.P. Trease, S.P. Magleby, L.L. Howell, Accommodating thickness in Origami-based deployable arrays1, Trans. ASME, J. Mech. Des. 135 (2013) 1–11, http://dx.doi.org/10.1115/1.4025372.

[3] M. Schenk, A.D. Viquerat, K.A. Seffen, S.D. Guest, Review of inflatable booms for deployable space structures: Packing and rigidization, J. Spacecr. Rockets 51 (2014) 762–778, http://dx.doi.org/10.2514/1.A32598.

[4] H. Fang, K. Wang, S. Li, Asymmetric energy barrier and mechanical diode effect from folding multi-stable stacked-Origami, Extreme Mech. Lett. 17 (2017) 7–15, http://dx.doi.org/10.1016/j.eml.2017.09.008.

[5] J. Tao, S. Li, Asymmetric multi-stability from relaxing the rigid-folding conditions in a stacked miura-ori cellular solid, Thin-Walled Struct. 179 (2022) http://dx.doi.org/10.1016/j.tws.2022.109685.

[6] M. Schenk, S.D. Guest, Geometry of Miura-folded metamaterials, Proc. Natl. Acad. Sci. USA 110 (2013) 3276–3281, http://dx.doi.org/10.1073/pnas.1217998110.

[7] E.T. Filipov, T. Tachi, G.H. Paulino, Origami tubes assembled into stiff, yet reconfigurable structures and metamaterials, Proc. Natl. Acad. Sci. 112 (2015) 12321–12326, http://dx.doi.org/10.1073/pnas.1509465112.

[8] Y. Zhang, Z. Yan, K. Nan, D. Xiao, Y. Liu, H. Luan, H. Fu, X. Wang, Q. Yang, J. Wang, W. Ren, H. Si, F. Liu, L. Yang, H. Li, J. Wang, X. Guo, H. Luo, L. Wang, Y. Huang, J.A. Rogers, A mechanically driven form of Kirigami as a route to 3D mesostructures in micro/nanomembranes, Proc. Natl. Acad. Sci. USA 112 (2015) 11757–11764, http://dx.doi.org/10.1073/pnas.1515602112.

[9] J. Kaufmann, P. Bhovad, S. Li, Harnessing the multistability of Kresling Origami for reconfigurable articulation in soft robotic arms, Soft Robot. 00 (2021) 1–12, http://dx.doi.org/10.1089/soro.2020.0075.

[10] M. Yu, W. Yang, Y. Yu, X. Cheng, Z. Jiao, A crawling soft robot driven by pneumatic foldable actuators based on miura-ori, Actuators 9 (2020) http://dx.doi.org/10.3390/ACT9020026.

[11] M. Johnson, Y. Chen, S. Hovet, S. Xu, B. Wood, H. Ren, J. Tokuda, Z.T.H. Tse, Fabricating biomedical Origami: A state-of-the-art review, Int. J. Comput. Assist. Radiol. Surg. 12 (2017) 2023–2032, http://dx.doi.org/10.1007/s11548-017-1545-1.

[12] C.L. Randall, E. Gultepe, D.H. Gracias, Self-folding devices and materials for biomedical applications, Trends Biotechnol. 30 (2012) 138–146, http://dx.doi.org/10.1016/j.tibtech.2011.06.013.

[13] P. Wang, T.A. Meyer, V. Pan, P.K. Dutta, Y. Ke, The beauty and utility of DNA Origami, Chem 2 (2017) 359–382, http://dx.doi.org/10.1016/j.chempr.2017.02.009.

[14] Y. Chen, J. Yan, J. Feng, Geometric and kinematic analyses and novel characteristics of Origami-inspired structures, Symmetry 11 (2019) http://dx.doi.org/10.3390/sym11091101.

[15] L.M. Fonseca, G.V. Rodrigues, M.A. Savi, An overview of the mechanical description of Origami-inspired systems and structures, Int. J. Mech. Sci. 223 (2022) http://dx.doi.org/10.1016/j.ijmecsci.2022.107316.

[16] N. Kidambi, K.W. Wang, Dynamics of Kresling Origami deployment, 2020, pp. 1–32, ArXiv.

[17] Y. Zhu, M. Schenk, E.T. Filipov, A review on Origami simulations: From kinematics, to mechanics, toward multiphysics, Appl. Mech. Rev. 74 (2022) http://dx.doi.org/10.1115/1.4055031.

[18] E.A. Peraza-Hernandez, D.J. Hartl, R.J. Malak, D.C. Lagoudas, Origami-inspired active structures: A synthesis and review, Smart Mater. Struct. 23 (2014) http://dx.doi.org/10.1088/0964-1726/23/9/094001.

[19] M. Meloni, J. Cai, Q. Zhang, D. Sang-Hoon Lee, M. Li, R. Ma, T.E. Parashkevov, J. Feng, Engineering Origami: A comprehensive review of recent applications, design methods, and tools, Adv. Sci. 8 (13) (2021) 2000636, http://dx.doi.org/10.1002/advs.202000636.

[20] D. Rus, M.T. Tolley, Design, fabrication and control of Origami robots, Nat. Rev. Mater. 3 (6) (2018) 101–112, http://dx.doi.org/10.1038/s41578-018-0009-8.

[21] T. Tachi, The method for judging rigid foldability, Origami 4 (2011) 177–186, http://dx.doi.org/10.1201/b10653-20.

[22] S. Waitukaitis, R. Menaut, B.G. ge Chen, M. van Hecke, Origami multistability: From single vertices to metasheets, Phys. Rev. Lett. 114 (2015) 055503, http://dx.doi.org/10.1103/PhysRevLett.114.055503.

[23] V. Brunck, F. Lechenault, A. Reid, M. Adda-Bedia, Elastic theory of Origami-based metamaterials, Phys. Rev. E 93 (2016) http://dx.doi.org/10.1103/PhysRevE.93.033005.

[24] S. Li, H. Fang, K.W. Wang, Recoverable and programmable collapse from folding pressurized Origami cellular solids, Phys. Rev. Lett. 117 (2016) 114301, http://dx.doi.org/10.1103/PhysRevLett.117.114301.

[25] S. Sadeghi, S. Allison, B. Betsill, S. Li, Exploiting the nonlinear stiffness of TMP Origami folding to enhance robotic jumping performance, Extreme Mech. Lett. (2020) 1–29.

[26] N. Baharisangari, S. Li, Exploiting the asymmetric energy barrier in multi-stable Origami to enable mechanical diode behavior in compression, in: Proceedings of the ASME Design Engineering Technical Conference, Vol. 5B-2019, 2019, pp. 1–8, http://dx.doi.org/10.1115/DETC2019-97420.

[27] H. Fang, S. Li, H. Ji, K.W. Wang, Dynamics of a bistable Miura-Origami structure, Phys. Rev. E 95 (2017) 052211, http://dx.doi.org/10.1103/PhysRevE.95.052211.

[28] M. Thota, S. Li, K.W. Wang, Lattice reconfiguration and phononic band-gap adaptation via Origami folding, Phys. Rev. B 95 (2017) http://dx.doi.org/10.1103/PhysRevB.95.064307.

[29] J.L. Silverberg, J.-H. Na, A.A. Evans, B. Liu, T.C. Hull, C.D. Santangelo, R.J. Lang, R.C. Hayward, I. Cohen, Origami structures with a critical transition to bistability arising from hidden degrees of freedom, Nature Mater. 14 (2015) 389–393, http://dx.doi.org/10.1038/nmat4232.

[30] B. Liu, J.L. Silverberg, A.A. Evans, C.D. Santangelo, R.J. Lang, T.C. Hull, I. Cohen, Topological kinematics of Origami metamaterials, Nat. Phys. 14 (2018) 811–815, http://dx.doi.org/10.1038/s41567-018-0150-8.

[31] S. Li, K.W. Wang, Fluidic Origami: A plant-inspired adaptive structure with shape morphing and stiffness tuning, Smart Mater. Struct. 24 (2015) 105031, http://dx.doi.org/10.1088/0964-1726/24/10/105031.

[32] K. Liu, G.H. Paulino, Nonlinear mechanics of non-rigid Origami: An efficient computational approach, Proc. R. Soc. A: Math. Phys. Eng. Sci. 473 (2017) http://dx.doi.org/10.1098/rspa.2017.0348.

[33] A. Gillman, K. Fuchi, P.R. Buskohl, Truss-based nonlinear mechanical analysis for Origami structures exhibiting bifurcation and limit point instabilities, Int. J. Solids Struct. 147 (2018) 80–93, http://dx.doi.org/10.1016/j.ijsolstr.2018.05.011.

[34] A.A. Evans, J.L. Silverberg, C.D. Santangelo, Lattice mechanics of Origami tessellations, Phys. Rev. E - Stat. Nonlinear Soft Matter Phys. 92 (2015) http://dx.doi.org/10.1103/PhysRevE.92.013205.

[35] J. Kaufmann, P. Bhovad, S. Li, Harnessing the multistability of Kresling Origami for reconfigurable articulation in soft robotic arms, Soft Robot. 9 (2) (2022) 212–223, http://dx.doi.org/10.1089/soro.2020.0075.

[36] J. Tao, S. Li, A study of the multi-stability in a non-rigid stacked Miura-Origami cellular mechanism, in: Proceedings of the ASME Design Engineering Technical Conference, Vol. 8B-2021, 2021, pp. 1–9, http://dx.doi.org/10.1115/DETC2021-67670.

[37] C. Jianguo, D. Xiaowei, Z. Ya, F. Jian, T. Yongming, Bistable behavior of the cylindrical Origami structure with Kresling pattern, Trans. ASME, J. Mech. Des. 137 (2015) 1DUMMMY, http://dx.doi.org/10.1115/1.4030158.

[38] Y. Zhu, E.T. Filipov, A bar and hinge model for simulating bistability in Origami structures with compliant creases, J. Mech. Robot. 12 (2020) http://dx.doi.org/10.1115/1.4045955.

[39] Y. Zhu, E.T. Filipov, An efficient numerical approach for simulating contact in Origami assemblages, Proc. R. Soc. A: Math. Phys. Eng. Sci. 475 (2019) http://dx.doi.org/10.1098/rspa.2019.0366.

[40] J.A. Faber, A.F. Arrieta, A.R. Studart, Bioinspired spring Origami, Science (2018) http://dx.doi.org/10.1126/science.aap775.

[41] M. Schenk, S.D. Guest, Origami folding: A structural engineering approach, 2011.

[42] Z.Y. Wei, Z.V. Guo, L. Dudte, H.Y. Liang, L. Mahadevan, Geometric mechanics of periodic pleated Origami, Phys. Rev. Lett. 110 (2013) 1–5, http://dx.doi.org/10.1103/PhysRevLett.110.215501, Anout origami, just wait..

[43] H. Zhang, H. Feng, J.L. Huang, J. Paik, Generalized modeling of Origami folding joints, Extreme Mech. Lett. 45 (2021) http://dx.doi.org/10.1016/j.eml.2021.101213.

[44] P. Bhovad, S. Li, Physical reservoir computing with Origami and its application to robotic crawling, Sci. Rep. 11 (2021) http://dx.doi.org/10.1038/s41598-021-92257-1.

[45] Y. Xia, E. Filipov, K.-W. Wang, The deployment dynamics and multistability of tubular fluidic Origami, Proc. SPIE (2021) 22, http://dx.doi.org/10.1117/12.2583500.

[46] S. Dong, Y. Yu, Numerical and experimental studies on capturing behaviors of the inflatable manipulator inspired by fluidic Origami structures, Eng. Struct. 245 (2021) http://dx.doi.org/10.1016/j.engstruct.2021.112840.

[47] S. Dong, X. Zhao, Y. Yu, Dynamic unfolding process of Origami tessellations, Int. J. Solids Struct. 226–227 (2021) http://dx.doi.org/10.1016/j.ijsolstr.2021.111075.

[48] B. Wang, C. Zhou, The imperfection-sensitivity of Origami crash boxes, Int. J. Mech. Sci. 121 (2017) 58–66, http://dx.doi.org/10.1016/j.ijmecsci.2016.11.027.

[49] J. Ma, Z. You, Energy absorption of thin-walled square tubes with a prefolded Origami pattern - part I: Geometry and numerical simulation, J. Appl. Mech. Trans. ASME 81 (2014) http://dx.doi.org/10.1115/1.4024405.

[50] K. Yang, S. Xu, J. Shen, S. Zhou, Y.M. Xie, Energy absorption of thin-walled tubes with pre-folded Origami patterns: Numerical simulation and experimental verification, Thin-Walled Struct. 103 (2016) 33–44, http://dx.doi.org/10.1016/j.tws.2016.02.007.

[51] S. Heimbs, P. Middendorf, S. Kilchert, A.F. Johnson, M. Maier, Experimental and numerical analysis of composite folded sandwich core structures under compression, Appl. Compos. Mater. 14 (2007) 363–377, http://dx.doi.org/10.1007/s10443-008-9051-9.

[52] S. Heimbs, J. Cichosz, M. Klaus, S. Kilchert, A.F. Johnson, Sandwich structures with textile-reinforced composite foldcores under impact loads, Compos. Struct. 92 (2010) 1485–1497, http://dx.doi.org/10.1016/j.compstruct.2009.11.001.
[53] X.M. Xiang, G. Lu, Z. You, Energy absorption of Origami inspired structures and materials, Thin-Walled Struct. 157 (2020) http://dx.doi.org/10.1016/j.tws.2020.107130.
[54] E.T. Filipov, G.H. Paulino, T. Tachi, Origami tubes with reconfigurable polygonal cross-sections, Proc. R. Soc. A: Math. Phys. Eng. Sci. 472 (2016) http://dx.doi.org/10.1098/rspa.2015.0607.
[55] K. Hayakawa, M. Ohsaki, The world congress of structural and multidisciplinary optimization, optimization approach to form generation of rigid-foldable Origami for deployable roof structure, in: World Congress of Structural and Multidisciplinary Optimization, 2019, pp. 1–2.
[56] X.M. Xiang, Z. You, G. Lu, Rectangular sandwich plates with Miura-ori folded core under quasi-static loadings, Compos. Struct. 195 (2018) 359–374, http://dx.doi.org/10.1016/j.compstruct.2018.04.084.
[57] P.T. Thai, M. Savchenko, I. Hagiwara, Finite element simulation of robotic Origami folding, Simul. Model. Pract. Theory 84 (2018) 251–267, http://dx.doi.org/10.1016/j.simpat.2018.03.004.
[58] J. Cai, Z. Ren, Y. Ding, X. Deng, Y. Xu, J. Feng, Deployment simulation of foldable Origami membrane structures, Aerosp. Sci. Technol. 67 (2017) 343–353, http://dx.doi.org/10.1016/j.ast.2017.04.002.
[59] D. Karagiozova, J. Zhang, G. Lu, Z. You, Dynamic in-plane compression of Miura-Ori patterned metamaterials, Int. J. Impact Eng. 129 (2019) 80–100, http://dx.doi.org/10.1016/j.ijimpeng.2019.02.012.
[60] A.A. Shabana, Definition of the slopes and the finite element absolute nodal coordinate formulation, Multibody Syst. Dyn. 1 (1997) 339–348, http://dx.doi.org/10.1023/A:1009740800463.
[61] A.M. Mikkola, A.A. Shabana, A non-incremental finite element procedure for the analysis of large deformation of plates and shells in mechanical system applications, Multibody Syst. Dyn. 9 (2003) 283–309, http://dx.doi.org/10.1023/A:1022950912782.
[62] B.A. Hussein, H. Sugiyama, A.A. Shabana, Coupled deformation modes in the large deformation finite-element analysis: Problem definition, J. Comput. Nonlinear Dyn. 2 (2007) 146–154, http://dx.doi.org/10.1115/1.2447353.
[63] H. Sugiyama, J. Gerstmayr, A.A. Shabana, Deformation modes in the finite element absolute nodal coordinate formulation, J. Sound Vib. 298 (2006) 1129–1149, http://dx.doi.org/10.1016/j.jsv.2006.06.037.
[64] A.E. Eldeeb, D. Zhang, A.A. Shabana, Cross-section deformation, geometric stiffening, and locking in the nonlinear vibration analysis of beams, Nonlinear Dynam. (2022) http://dx.doi.org/10.1007/s11071-021-07102-x.
[65] O.N. Dmitrochenko, B.A. Hussein, A.A. Shabana, Coupled deformation modes in the large deformation finite element analysis: Generalization, J. Comput. Nonlinear Dyn. 4 (2009) 1–8, http://dx.doi.org/10.1115/1.3079682.
[66] A.A. Shabana, C.J. Desai, E. Grossi, M. Patel, Generalization of the strain-split method and evaluation of the nonlinear ANCF finite elements, Acta Mech. 231 (2020) 1365–1376, http://dx.doi.org/10.1007/s00707-019-02558-w.
[67] C.M. Pappalardo, M. Wallin, A.A. Shabana, A new Ancf/CRBF fully parameterized plate finite element, J. Comput. Nonlinear Dyn. 12 (2017) 1–13, http://dx.doi.org/10.1115/1.4034492.
[68] A.A. Shabana, Justifications for using ancf finite elements, University of Illinois at Chicago, Chicago, 2022, pp. 1–18, http://dx.doi.org/10.25417/uic.20999116.v1.
[69] L.P. Obrezkov, M.K. Matikainen, A.B. Harish, A finite element for soft tissue deformation based on the absolute nodal coordinate formulation, Acta Mech. 231 (2020) 1519–1538, http://dx.doi.org/10.1007/s00707-019-02607-4.
[70] L. Ma, C. Wei, C. Ma, Y. Zhao, Modeling and verification of a RANCF fluid element based on cubic rational Bezier volume, J. Comput. Nonlinear Dyn. 15 (2020) http://dx.doi.org/10.1115/1.4046206.
[71] M. Berzeri, A.A. Shabana, Development of simple models for the elastic forces in the absolute nodal co-ordinate formulation, J. Sound Vib. 235 (2000) 539–565, http://dx.doi.org/10.1006/jsvi.1999.2935.
[72] K. Otsuka, K. Makihara, H. Sugiyama, Recent advances in the absolute nodal coordinate formulation: Literature review from 2012 to 2020, J. Comput. Nonlinear Dyn. 17 (2022) http://dx.doi.org/10.1115/1.4054113.
[73] K. Nachbagauer, State of the art of ANCF elements regarding geometric description, interpolation strategies, definition of elastic forces, validation and the locking phenomenon in comparison with proposed beam finite elements, Arch. Comput. Methods Eng. 21 (2014) 293–319, http://dx.doi.org/10.1007/s11831-014-9117-9.
[74] J. Bonet, R.D. Wood, Nonlinear Continuum Mechanics for Finite Element Analysis, Vol. 9780521838, Second Ed., Cambridge University Press, 2008, pp. 1–318, http://dx.doi.org/10.1017/CBO9780511755446.
[75] A.J.M. Spencer, Continuum Mechanics, Dover Publications, 2004.
[76] K. Dufva, A.A. Shabana, Analysis of thin plate structures using the absolute nodal coordinate formulation, Proc. Inst. Mech. Eng. Part K: J. Multi-Body Dyn. 219 (2005) 345–355, http://dx.doi.org/10.1243/146441905X50678.
[77] L.P. Obrezkov, A. Mikkola, M.K. Matikainen, Performance review of locking alleviation methods for continuum ANCF beam elements, Nonlinear Dynam. 109 (2022) 531–546, http://dx.doi.org/10.1007/s11071-022-07518-z.
[78] M. Patel, A.A. Shabana, Locking alleviation in the large displacement analysis of beam elements: The strain split method, Acta Mech. 229 (2018) 2923–2946, http://dx.doi.org/10.1007/s00707-018-2131-5.
[79] K. Nachbagauer, A.S. Pechstein, H. Irschik, J. Gerstmayr, A new locking-free formulation for planar, shear deformable, linear and quadratic beam finite elements based on the absolute nodal coordinate formulation, Multibody Syst. Dyn. 26 (2011) 245–263, http://dx.doi.org/10.1007/s11044-011-9249-8.
[80] J. Gerstmayr, A.A. Shabana, Analysis of thin beams and cables using the absolute nodal co-ordinate formulation, Nonlinear Dynam. 45 (2006) 109–130, http://dx.doi.org/10.1007/s11071-006-1856-1.
[81] A.A. Shabana, Computational Continuum Mechanics, Wiley, 2018.
[82] A.M. Recuero, J.F. Aceituno, J.L. Escalona, A.A. Shabana, A nonlinear approach for modeling rail flexibility using the absolute nodal coordinate formulation, Nonlinear Dynam. 83 (2016) 463–481, http://dx.doi.org/10.1007/s11071-015-2341-5.
[83] A. Shabana, Dynamics of Multibody Systems, fifth ed., Cambridge University Press, New York, 2020.
[84] C. Lv, D. Krishnaraju, G. Konjevod, H. Yu, H. Jiang, Origami based mechanical metamaterials, Sci. Rep. 4 (2014) http://dx.doi.org/10.1038/srep05979.
[85] M.A. Ablat, A. Qattawi, Finite element analysis of Origami-based sheet metal folding process, J. Eng. Mater. Technol. Trans. ASME 140 (2018) http://dx.doi.org/10.1115/1.4039505.